Supporting information

Synthesis, crystal structure and photocatalytic properties of two isoreticular Ce(IV)-MOFs with an infinite rod-shaped inorganic building unit

Jonas Gosch,[a] Diletta Morelli Venturi,[b] Erik Svensson Grape,[c] Cesare Atzori,[d] Lorenzo Donà,[e] Felix Steinke,[a] Tobias Otto,[a] Tim Tjardts,[f] Bartolomeo Civalleri,[e] Kirill A. Lomachenko,[d] A. Ken Inge,[c] Ferdinando Costantino*,[b] and Norbert Stock*,[a,g]

[a] Institut für Anorganische Chemie, Christian-Albrechts-Universität zu Kiel, Max-Eyth-Str. 2, 24118 Kiel, Germany.

[b] Dipartimento di Chimica Biologia e Biotecnologia, University of Perugia, Via Elce di Sotto 8, 06123 Perugia, Italy.

[c] Department of Materials and Environmental Chemistry, Stockholm University, Svante Arrhenius väg 16C, 106 91 Stockholm, Sweden.

[d] European Synchrotron Radiation Facility, 71 avenue des Martyrs, 38043 Grenoble Cedex 9, France.

[e] Dipartimento di Chimica, Università degli Studi di Torino, Via P. Giuria 7, 10125 Turin, Italy.

[f] Technische Fakultät, Christian-Albrechts-Universität zu Kiel, Kaiserstraße 2, 24143 Kiel, Germany.

[g] Kiel Nano, Surface and Interface Science KiNSIS, Christian-Albrechts-Universität zu Kiel, Christian-Albrechts-Platz 4, 24118 Kiel, Germany.

* corresponding authors

Norbert Stock: stock@ac.uni-kiel.de

Ferdinando Costantino: ferdinando.costantino@unipg.it

Table of contents

1. Materials and methods

Cerium(IV) ammonium nitrate ($(NH_4)_2[Ce(NO_3)_6]$, ABCR, 98 %), 4,4'-oxydibenzoic acid (H_2ODB, TCI, 98 %), 4,4'-carbonyldibenzoic acid (H_2CDB, TCI, >95 %) and methyl orange (Merck) were obtained commercially and used without further purification. Syntheses were carried out in an Anton Paar Synthos 3000 microwave oven in glass tubes ($V_{max} = 3$ mL) under stirring. Optimized syntheses were carried out in 20 mL glass reactors using a Biotage® Initiator and Initiator+ microwave system. Since the heating in the 3 mL glass vials is indirectly accomplished through the microwave assisted heating of a SiC sample holder, the temperature in the glass vials may show some deviations to the monitored temperature.[1] In contrast, in the scale-up, direct heating is used and the reaction temperature is measure by an IR detector at the surface of the glass vessel. Powder X-ray diffraction (PXRD) data was collected on a STOE STADI P diffractometer equipped with a MYTHEN 1 K detector ($CuK_{\alpha 1}$-radiation, $\lambda = 1.5406$ Å). 3D ED data were collected using a continuous rotation approach (see Section S3 for details). Elemental analyses were performed with a vario MICRO cube Elementaranalysator from Elementar. IR spectra were recorded at room temperature on a Bruker Vertex70 FT-IR spectrometer using a broadband spectral range extension VERTEX FM for full mid and far IR in the range of 6.000-80 cm^{-1}. For diffuse reflectance infrared Fourier transform spectroscopy (DRIFTS) the device was equipped with a Praying Mantis™ Diffuse Reflection Accessory and a High Temperature Reaction Chamber by Harrick Scientific Products. Thermogravimetric (TG) and differential thermal analysis (DTA) data were collected on a Linseis STA PT 1000 (airflow = 6 Lh^{-1}, heating rate = 4 K min^{-1}). Variable temperature PXRD data (VT-PXRD) were collected with a STOE capillary furnace in 0.5 mm quartz capillaries. The temperature range between 30 °C and the decomposition temperatures of the title compounds were studied. The samples were heated in steps of 10 or 20 °C (heating rate: 50 °C/min, measurement time: 10 min). Sorption measurements were carried out using a BEL Japan Inc. BELSORP-max apparatus with nitrogen gas and water vapor at 77 and 298 K, respectively. The samples were treated for 16 h at a temperature of 210 °C under reduced pressure ($p < 10^{-2}$ mbar) prior to the measurements. Scanning electron micrographs (SEM) of microcrystalline powders were collected on a Zeiss Supra 55 VP. Samples were previously sputtered with gold to enhance conductivity and resolution.

The oxidation state of the metal ions of the Ce-MOFs in the bulk were determined by analyzing the X-ray absorption spectroscopy near edge structure (XANES) at the Ce L_3-edge at BM23 beamline[2] of the European Synchrotron Radiation Facility (Grenoble, France). The measurements were conducted in transmission mode using a Si(111) double-crystal monochromator and three N_2/He-filled ionization chambers. Two flat Si mirrors positioned at the incidence angle of 4 mrad were used for harmonics rejection. Energy calibration was ensured by measuring the spectra of CeO_2 simultaneously with the samples using the third ionization chamber. All samples were diluted with boron nitride and measured at room temperature in the form of self-supporting pellets. The mass of the pellets was optimized for the best signal-to-noise ratio employing the XAFSmass code.[3] Spectra of liquid samples after reaction with methyl orange were measured in fluorescence mode at 90° angle by the means of a 1-mm-thick SDD detector (Hitachi Vortex). Read out was made with a XIA FalconX signal processor and deadtime was kept below 15 %. XAS data treatment, including XANES linear combination analysis, was performed with the Athena code of the Demeter package.[4]

X-ray photoelectron spectroscopy (XPS, XPS UHV system from PREVAC Sp. z o. o., Al-anode, 300W) was applied to determine the oxidation state of incorporated Ce ions at the surface of the MOF particles. Survey scans were conducted at 3 iterations and a pass energy of 200 eV while high-resolution scans were performed at 20 iterations and a pass energy of 50 eV. For the analysis of XPS spectra, the software CasaXPS (version 2.3.23)[5] was used. To quantify the background of each spectrum the Shirley algorithm was used. Furthermore, all relevant photoemission peaks were fitted by a combination of Gaussian-Lorentzian model peaks. The charge correction was done by fitting the C 1s main peak and setting the peak position of the fit to 284.8 eV while adjusting all belonging spectra accordingly. Gas chromatography measurements were performed on an Agilent 6890 Plus gas chromatograph with Ar as the carrier gas, a 5 Å molecular sieve column and a thermal conductivity detector. During photocatalytic reactions, the pH was monitored with pH-indicator strips to pH 3.0–6.0. Dye concentration was quantified using UV-Vis spectroscopy on a Varian Cary 5000 UV-Vis-NIR spectrophotometer. For the additional experiments with varying amounts of catalyst, a Spectroquant UV-VIS (Pharo 300) spectrophotometer was used. The concentration of cerium ions in solution after the catalytic reactions were determined by a PerkinElmer Avio 200 ICP optical emission spectrometer equipped with a PerkinElmer S23 auto sampler.

2. Discovery of CAU-58-ODB and CAU-58-CDB

The first syntheses were carried out in an Anton Paar Synthos 3000 microwave oven in glass tubes (V_{max} = 3 mL) under stirring. Therefore, 27.5 mg (0.107 mmol) of 4,4'-oxydibenzoic acid (H_2ODB) or 28.8 mg (0.107 mmol) of 4,4'-carbonyldibenzoic acid (H_2CDB) were introduced into microwave glass reactors as solids and a solution of cerium(IV) ammonium nitrate in acetonitrile (800 µL, 1.333 M) was added. The reactors were sealed and heated for 5 h at 140 °C. After cooling to room temperature and a controlled pressure release, products were filtered off, washed three times with 3 mL *N,N*-dimethylformamide and acetone respectively and dried at air. CAU-58-ODB [CeO(H_2O)(ODB)] and CAU-58-CDB [CeO(H_2O)(CDB)] were obtained as microcrystalline powders of orange and yellow color. Syntheses were subsequently optimized and scaled up by a factor of 14 (see main manuscript).

3. Side reaction during the MOF syntheses

During MOF syntheses, gas evolution is observed that leads to a significant pressure buildup in the reaction vessel. The pressure was monitored by the Biotage Initiator+ microwave oven (Fig. S1) and partly remained even after cooling of the reaction mixture to room temperature. To understand the underlying reaction, the synthesis was repeated under the same conditions but without any linker molecule. A similar pressure buildup was observed proving that the gas evolution is not related to the respective MOF formation.
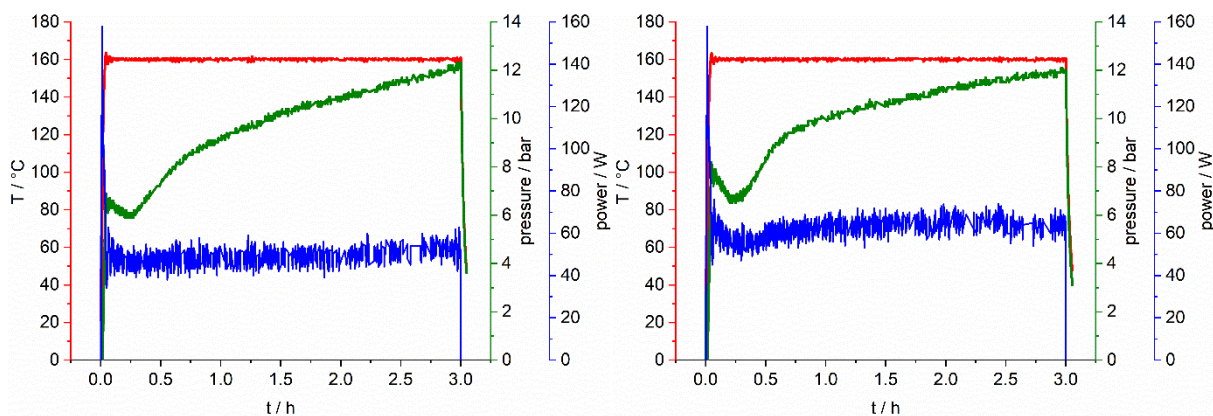
Figure S1. Temperature (red), pressure (green) and microwave power (blue) during the synthesis of CAU-58-CDB (left) and under the same conditions but without the linker (right).

In addition, simple experiments under different conditions revealed that this side reaction also occurs in other solvents (i.e. isopropanol) but disappears when using other Ce(IV) salts like Ce(SO$_4$)$_2$. The emerging gaseous species in the reaction vessel was further analyzed *via* gas chromatography (Fig. S2) and shows a high excess of N$_2$ (95.8 %) over O$_2$ (0.9 %) and gaseous acetonitrile (3.3 %).
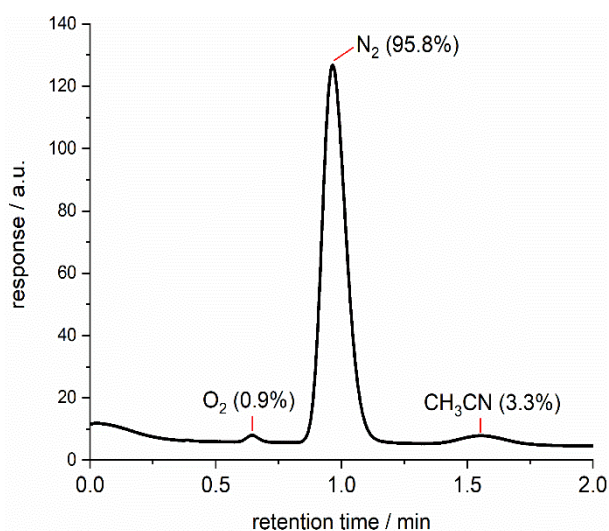

**Figure S2.** Gas chromatogram of the emerging gaseous species in the reaction vessel shows a high excess of N$_2$.

We therefore ascribe the formation of N$_2$ to a comproportionation reaction between nitrate and ammonium ions of ceric ammonium nitrate (CAN):

$$3\ NO_3^- + 5\ NH_4^+ \rightarrow 4\ N_2 + 9\ H_2O + 2\ H^+ \tag{1}$$
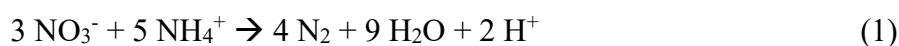
Apart from the evolution of nitrogen, the side reaction yields a significant amount of water, which leads to the hydrolysis of acetonitrile and the formation of acetamide:

$$H_2O + CH_3CN \rightarrow CH_3CONH_2 \tag{2}$$
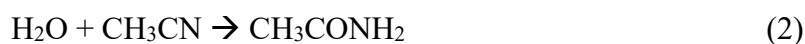
Acetamide could be detected by NMR spectroscopy from the reaction mixture without linker (Fig. S3). During the MOF syntheses, acetamide is usually removed by washing the MOF samples with DMF and acetone.
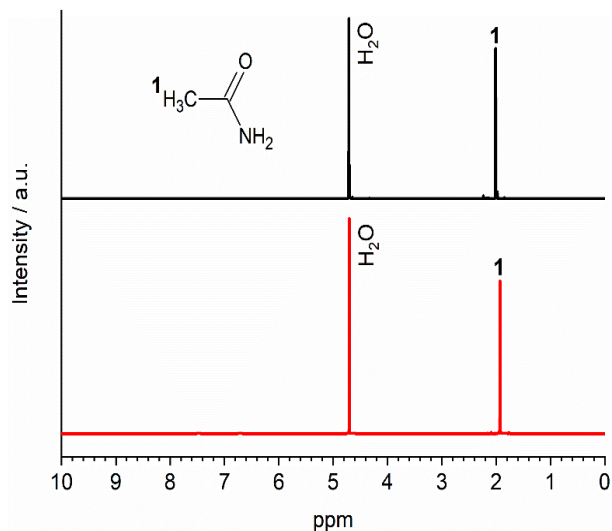
Figure S3. NMR spectra of observed acetamide in the reaction mixture (black) and commercially obtained acetamide (red) measured in D_2O.

4. Three-dimensional electron diffraction

Three-dimensional electron diffraction data of CAU-58-ODB was collected using a JEOL JEM2100 TEM, equipped with a Timepix detector from Amsterdam Scientific Instruments. The samples were prepared by sprinkling small amounts of the microcrystalline materials onto holey carbon covered copper grids. The data collection was carried out using Instamatic,[6] continuously rotating the crystal at a rate of $0.45 \,°s^{-1}$ with a subsequent reduction of the data being performed using XDS.[7] The acquired intensities were then used to solve the structures with SHELXT,[8] and refined using SHELXL,[9] with electron scattering factors extracted from SIR2014.[10] From the 3D ED data, all non-hydrogen atoms could be located in the initial structure solution. Crystallographic data from the electron diffraction measurements on CAU-58-ODB is presented in Table S1.

Table S1. Crystallographic data from electron diffraction measurements on CAU-58-ODB.

Parameter	Value
wavelength	0.0251 Å
crystal system	orthorhombic
space group	$P2_12_12_1$ (No. 19)
a / Å	7.24(4)
b / Å	14.64(7)
c / Å	30.18(15)
V / Å^3	3199(32)
Z	4
index ranges	$-8 \leq h \leq 8$ $-13 \leq k \leq 16$ $-37 \leq l \leq 37$
reflections collected	24682
independent reflections	5572
completeness (to 0.8 Å resolution)	91 %
R_{int}	0.2062
R_1 (ED model) [$I > 2\sigma(I)$]	0.3906

5. Structure of CAU-58-ODB

All indexing and refinement steps of the PXRD patterns described herein was carried out using TOPAS academic.[11]

Rietveld refinement of CAU-58-ODB

The crystal structure of CAU-58-ODB obtained from electron diffraction was used as a starting model for a Rietveld refinement against powder X-ray diffraction data. The lattice parameters obtained from a preceding indexing of the PXRD data were used instead of the lattice parameters obtained from electron diffraction data. For the structure refinement, Z-matrices for each linker were employed in order to refine the bond lengths of the linker molecules as well as the rotation of the phenylene rings and the carboxylate groups within given constraints. Distance restraints were set up to refine the Ce-O bonds. Adsorbed water molecules inside the pores were considered and refined as oxygen atoms on general positions. One temperature factor each was used for the atoms of the linker molecules, the cerium and oxygen atoms as part of the IBU as well as the guest molecules, respectively. Figure S4 shows the final results of the Rietveld refinement. The crystallographic data is given in Table 1 of the main manuscript. Selected bond lengths of the structure are summarized in Table S2.
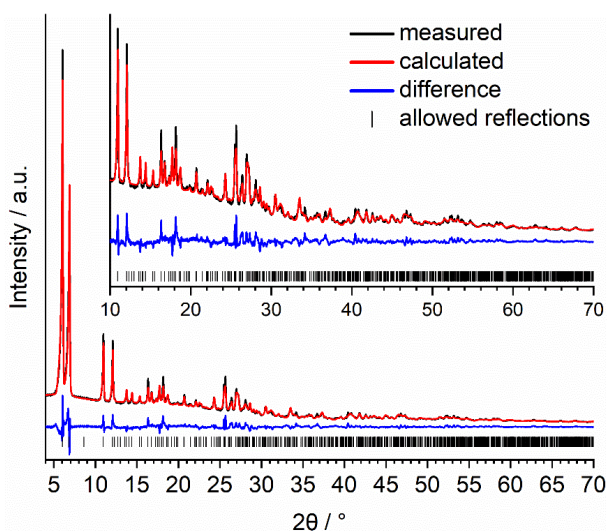
Figure S4. Rietveld refinement on the PXRD data (λ = 1.5401 Å) of CAU-58-ODB.

Table S2. Selected bond lengths in the crystal structure of CAU-58-ODB obtained from Rietveld refinement.

Atoms	Distance / Å	Atoms	Distance / Å
Ce1-O03	2.39(10)	Ce2-O03	2.39(11)
Ce1-O03	2.39(11)	Ce2-O04	2.32(13)
Ce1-O04	2.39(12)	Ce2-O05	2.51(7)
Ce1-O04	2.40(11)	Ce2-O06	2.53(12)
Ce1-O12	2.54(11)	Ce2-O11	2.51(9)
Ce1-O22	2.52(9)	Ce2-O12	2.54(9)
Ce1-O31	2.52(11)	Ce2-O21	2.55(3)
Ce1-O42	2.51(10)	Ce2-O32	2.55(9)
		Ce2-O41	2.55(3)
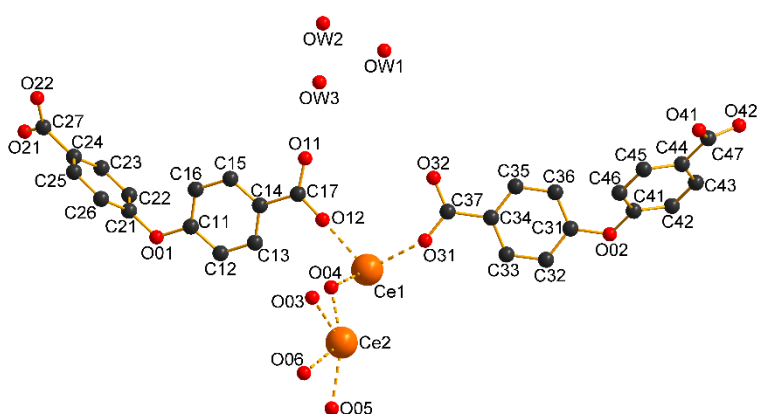
Figure S5. Asymmetric unit of [CeO(H_2O)(ODB)].

8

**Description of the rod-shaped IBU in CAU-58**

In the rod-shaped IBU of CAU-58 two symmetry independent Ce^{4+} ions are surrounded by eight and nine oxygen ions, respectively (Fig. S6). Four oxygen ions of the eightfold coordinated, as well as five oxygen ions of the ninefold coordinated Ce^{4+} ions can be assigned to the linker. The other four oxygen ions of the [CeO$_8$] polyhedra correspond to threefold bridging μ_3-O^{2-} ions with two of them also connected to the ninefold surrounded Ce^{4+} ion. The remaining two oxygen ions were identified as water molecules, which point into the pores of the structure. [CeO$_8$] polyhedra are linked alternatingly *via* edges to form the backbone of a chain. In addition, each chain link is extended by one face-linked [CeO$_9$] polyhedra orthogonal to the chain direction.
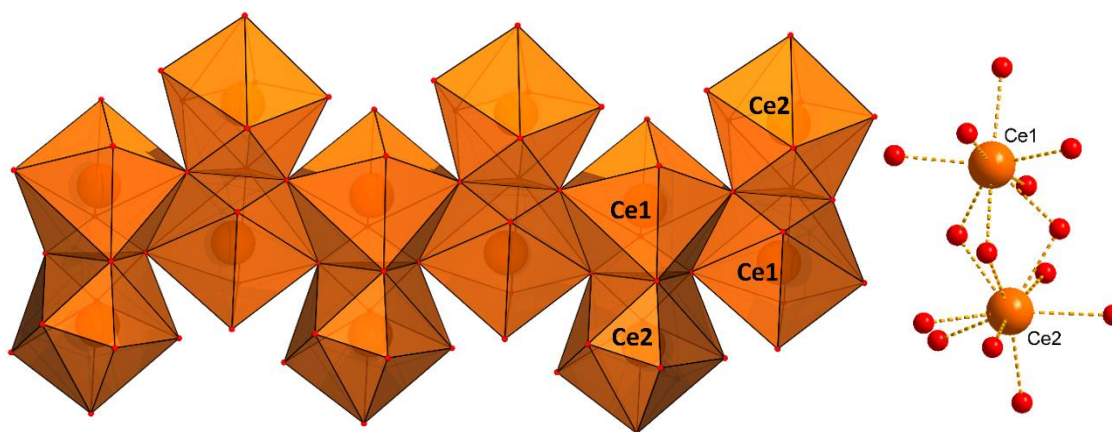
Figure S6. The IBU of CAU-58 is built up by edge- and face-sharing [CeO$_8$] and [CeO$_9$] polyhedra.

**Comparison of reported IBUs in Ce(IV)-MOF chemistry**
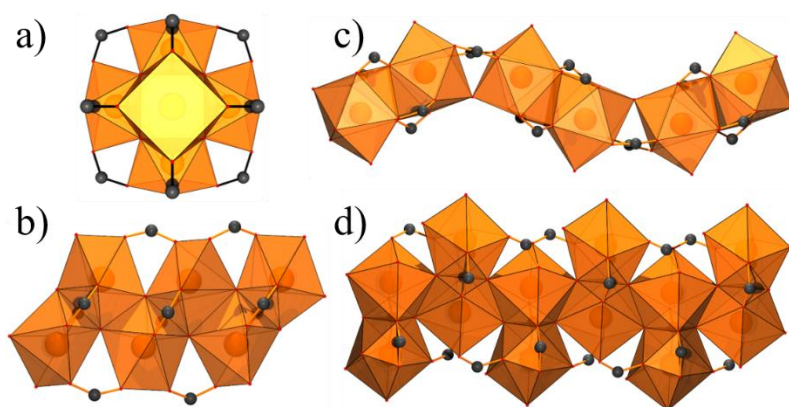
Figure S7. Inorganic building units of the UiO-66 (a),[12] MIL-140 (b),[13] CSUST-3 (c)[14] and CAU-58 structure type (d).

6. Structure of CAU-58-CDB

A comparison between the initial CAU-58-CDB_dry, the water treated CAU-58-CDB_wet and CAU-58-ODB is presented in Figure S8. Despite a broadening of the reflections, the diffraction pattern of CAU-58-CDB_wet is very similar to the one from CAU-58-ODB. Based on the crystal parameters of CAU-58-ODB, the PXRD data of CAU-58-CDB_wet could be successfully fitted using a LeBail-fit (Fig. S9, right). Indexing of the PXRD data from CAU-58-CDB_dry resulted in a monoclinic crystal system which was subsequently confirmed by a LeBail-fit (Fig. S9, left).
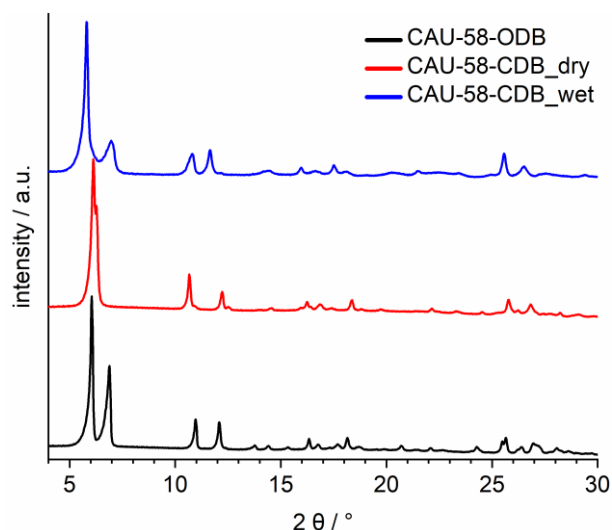

Figure S8. PXRD patterns (λ = 1.5401 Å) of CAU-58-ODB, CAU-58-CDB_dry and CAU-58-CDB_wet.
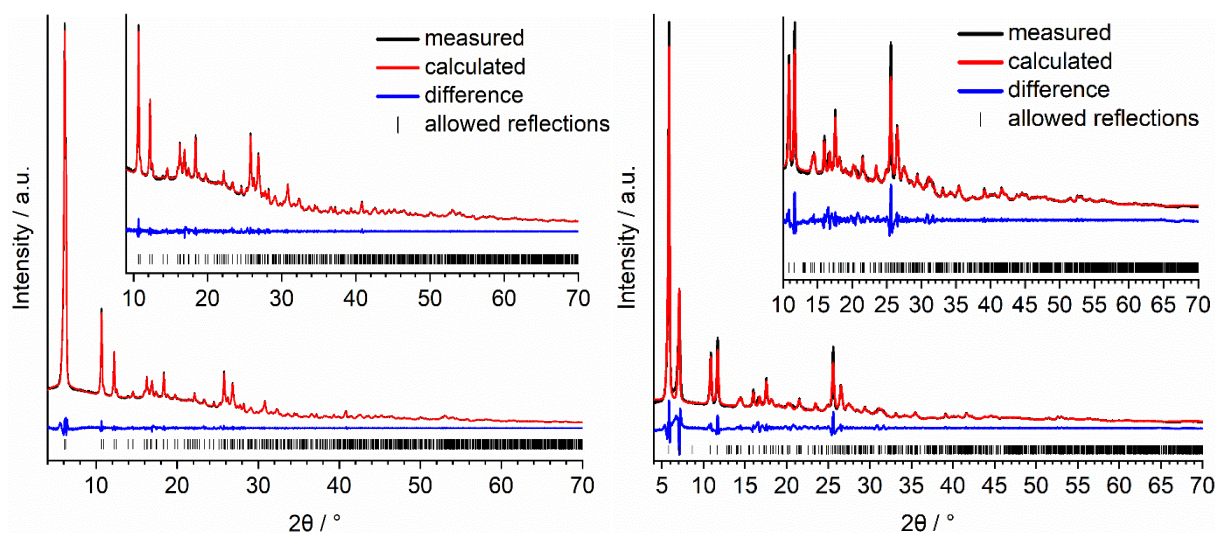
Figure S9. LeBail-Fit on the PXRD data (λ = 1.5401 Å) of CAU-58-CDB_dry (left). LeBail-Fit on the PXRD data (λ = 1.5401 Å) of CAU-58-CDB_wet using the crystal parameters of CAU-58-ODB (right).

10

7. Topological analysis

The topology of CAU-58-ODB can be visualized by using the points of extension approach previously described by Schoedel and coworkers.[15] Therefore, the MOF and the incorporated rod-shaped IBU need to be deconstructed. Points where the organic and inorganic parts of the MOF are connected are designated as nodes of the underlying net. For this, nodes are inserted into the structure on the position of each carboxylate group (Figure S10, left). For the deconstruction of the ODB^{2-} linker molecules, additional nodes are placed into each of the two benzene rings. The resulting net structure is displayed in Figure S10 (right).
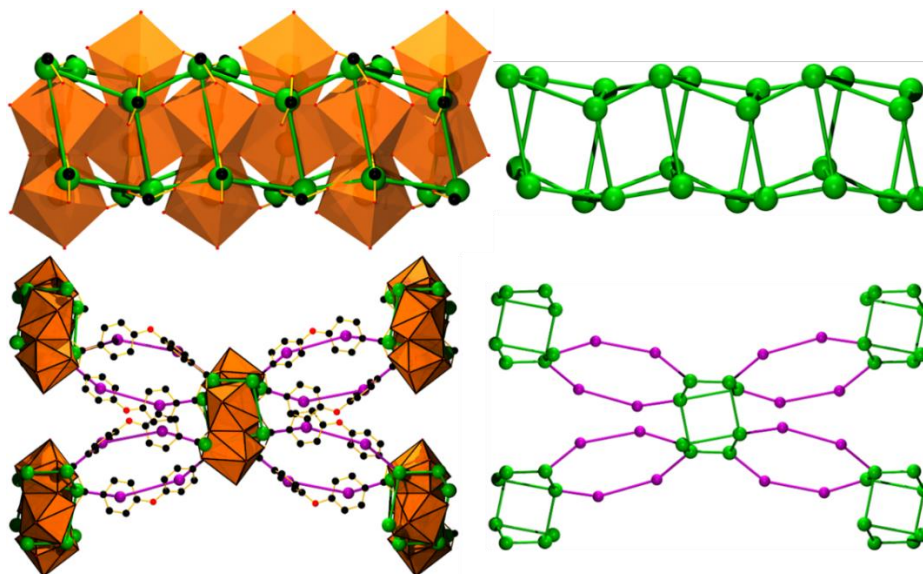

Figure S10. Representation of the topology of CAU-58-ODB using the point of extension approach with (left) and without the original structure (right).

For further simplification the crystal structure can be modified by using the programs ToposPro[16] and Systre (part of the Gavrog package).[17] Within this process the unnecessary 2-coordinated nodes are removed and bond lengths are unified (Figure S11). Topological analysis of the simplified net results in a uninodal 5-c net with the RCSC (Reticular Chemistry Structure Resource) code **fee** and the point symbol $\{4^7.6^3\}$.
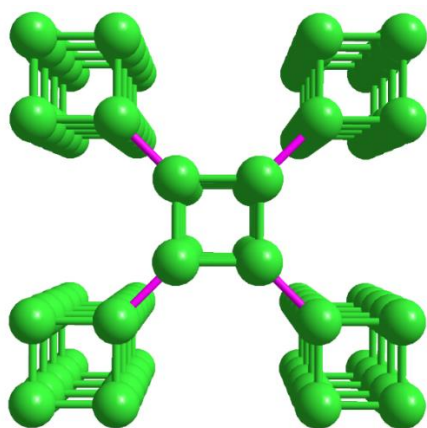
Figure S11. Simplified model of the underlying net in CAU-58-ODB using the point of extension approach.

8. Connolly Surface analysis
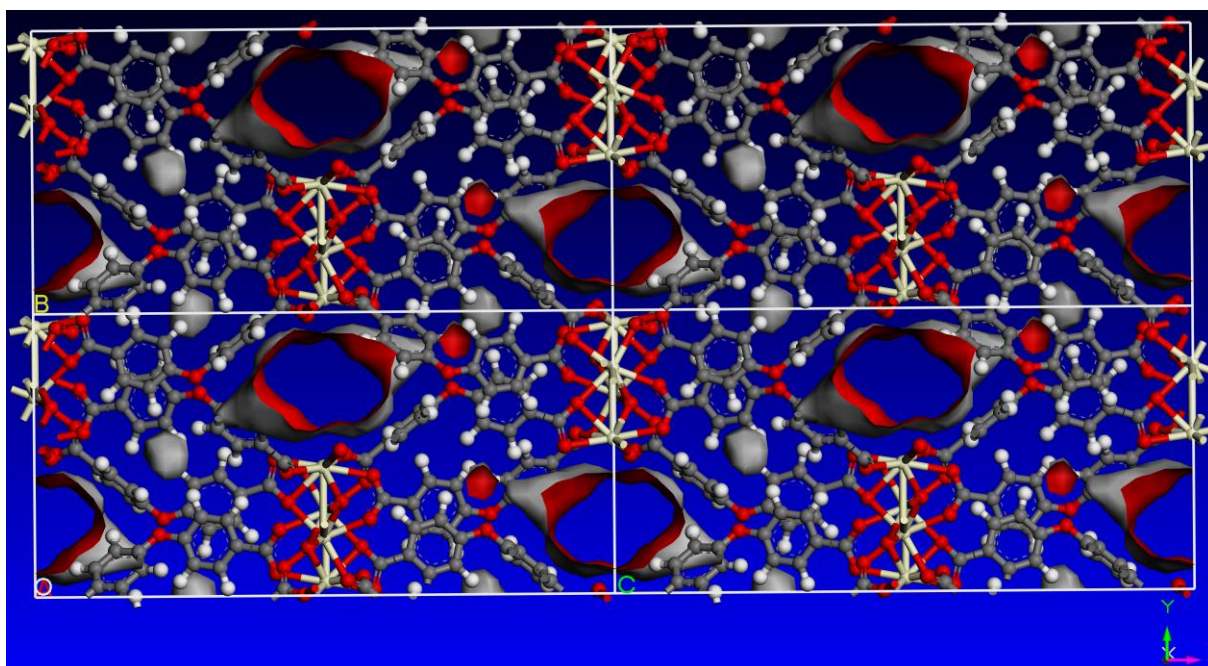
Figure S12. Connolly surface calculated for CAU-58-ODB. For the simulation, a water molecule (diameter: 2.6 Å) was employed as a probe molecule.

9. DFT calculations

Density Functional Theory (DFT) calculations were carried out with the cost-effective PBEsol0-3c method[18] recently developed by some of us and implemented in a development version of the CRYSTAL17[18] code.

In the PBEsol0-3c method, the total energy computed with the PBEsol0 hybrid functional combined with a double-ζ quality Gaussian basis set, is augmented with two semi-empirical corrections to remove the Basis Set Superposition Error (BSSE) through the geometrical CounterPoise (gCP)[19,20] approach and to properly describe weak interactions *via* the D3 scheme[21,22] in its Becke-Johnson rational damping variant. In the present work, the solid-state basis set adopted by the PBEsol0-3c composite method has been extended to treat Ce. The def2-SVP basis set of Ce has been modified according to the strategy described in the reference.[18]

The PBEsol0-3c hybrid composite method has been shown to accurately and efficiently describe inorganic systems and micro-mesoporous material,[23] including MOFs for which structural, vibrational, electronic and adsorption properties have been predicted with excellent results.[24] More recently, it has been also successfully applied to investigate the encapsulation of molecules in HKUST-1 and ZIF-8 for drug delivery (i.e. 5-fluorouracil),[25] and for solid state lighting (i.e. fluorescein)[26] respectively, as well as to elucidate the mechanical properties of defective ZIF-8.[24]

For the numerical evaluation of the Exchange-Correlation term a (75,974) pruned grid was employed, corresponding to the XLGRID keyword as used by the CRYSTAL code. Default convergence criteria for geometry optimization were employed. The tolerances for one- and two-electron integrals calculation were set to 10^{-7}, 10^{-7} for the Coulomb and to 10^{-7}, 10^{-7}, 10^{-25} for the Exchange series, respectively. The shrinking factors for the diagonalization of the Kohn-Sham matrix in the reciprocal space were set to 2 for the Monkhorst-Pack net and to 2 for the Gilat net, respectively. A full relaxation of both lattice parameters and atomic positions was performed and the crystal symmetry was maintained during the optimization process.

Single-point energy calculations have been carried out with the HSEsol-3c method[18] on the PBEsol0-3c optimized model systems for a better evaluation of the band gap.

Lattice parameters and unit cell volumes computed with the PBEsol0-3c composite method for CAU-58 MOFs are reported in Table S3.

Table S3. PBEsol0-3c computed lattice parameters of CAU-58-ODB, CAU-58-CDB_wet and CAU-58-CDB_dry. Two different hydrogen bonding patterns (*pattern-1* and *pattern-2*) have been simulated.

lattice parameters	CAU-58-ODB *pattern-1*	CAU-58-CDB_wet *pattern-1*	CAU-58-CDB_dry *pattern-1*
space group	$P2_12_12_1{}^*$	$P2_12_12_1{}^*$	$P2_1{}^*$
a / Å	6.932	6.917	6.908
b / Å	15.128	15.735	15.792
c / Å	29.231	29.243	29.274
β / °			89.93
V / Å^3	3065.23	3182.75	3193.43
lattice parameters	CAU-58-ODB *pattern-2*	CAU-58-CDB_wet *pattern-2*	CAU-58-CDB_dry *pattern-2*
space group	$P2_12_12_1{}^*$	$P2_12_12_1{}^*$	$P2_1{}^*$
a / Å	6.855	6.854	6.904
b / Å	15.382	16.355	15.715
c / Å	29.321	29.057	28.954
β / °			90.01
V / Å^3	3091.82	3256.93	3141.53

*All DFT calculations were carried out in the space group *P*1. Nevertheless the space groups from the evaluation of the PXRD data are given.

13

The PBEsol0-3c optimized structures for the two hydrogen bond patterns (*pattern-1* and *pattern-2*) of CAU-58-ODB, CAU-58-CDB_wet and CAU-58-CDB_dry are depicted below.
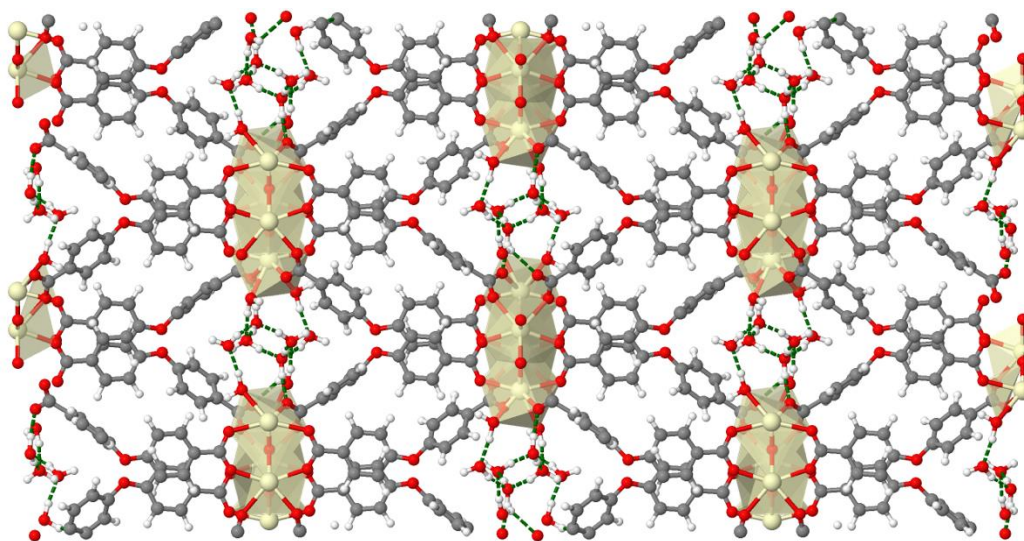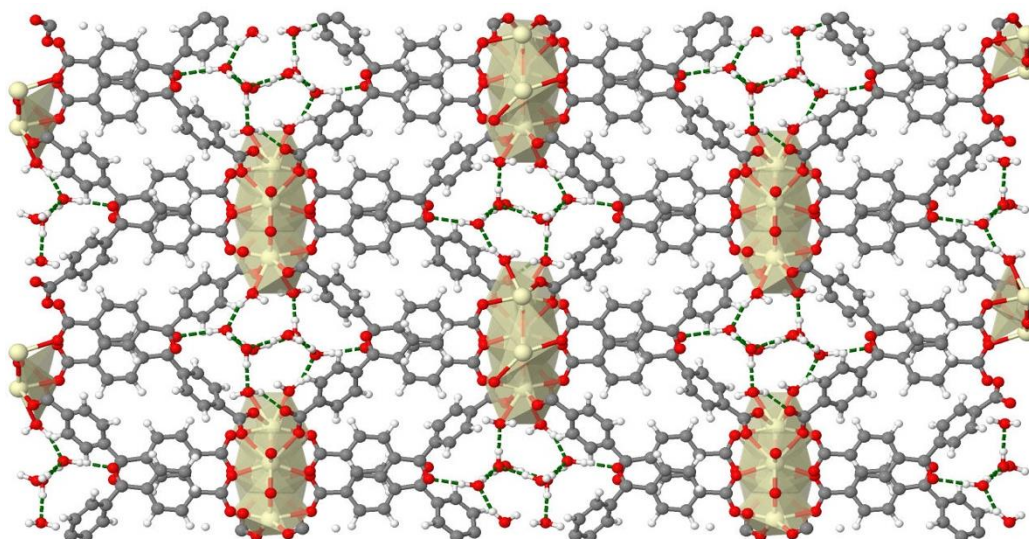

Figure S13. Crystal structure of CAU-58-ODB *pattern-1* obtained at the PBEsol0-3c level of theory. Color scheme: Ce and Ce-O polyhedra = yellow, O = red, C = grey, H = white. The hydrogen-bond network is represented by dashed green lines.
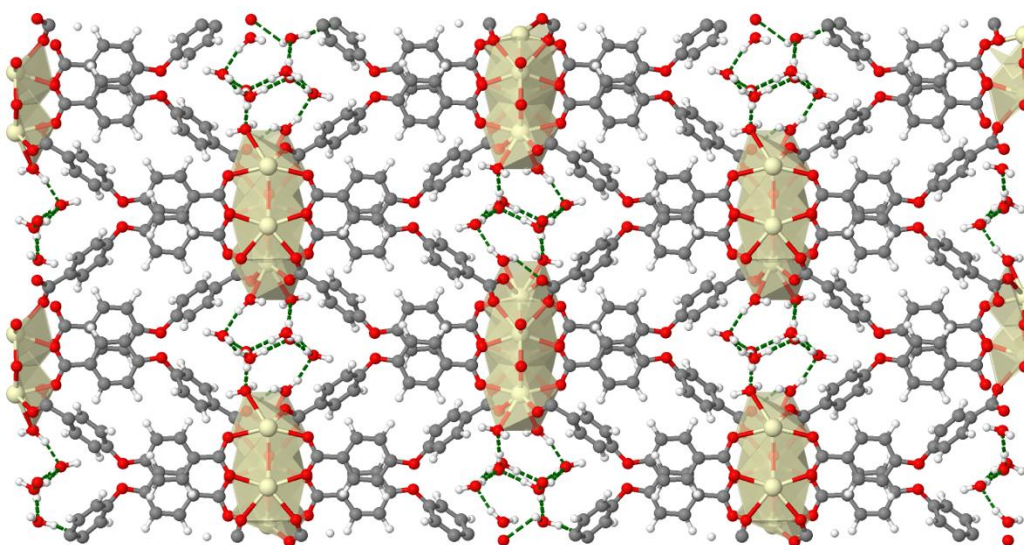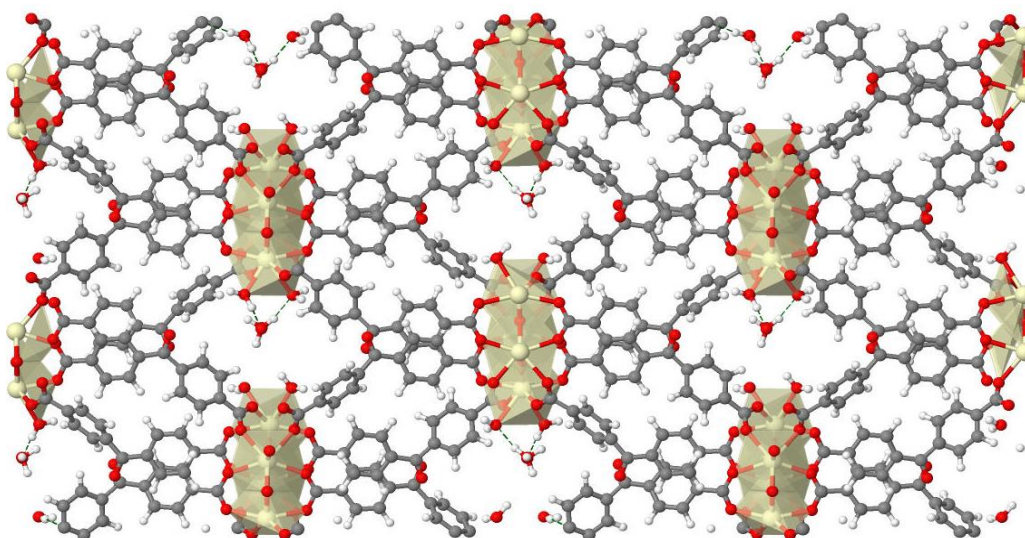

Figure S14. Crystal structure of CAU-58-ODB *pattern-2* obtained at the PBEsol0-3c level of theory. Color scheme: Ce and Ce-O polyhedra = yellow, O = red, C = grey, H = white. The hydrogen-bond network is represented by dashed green lines.
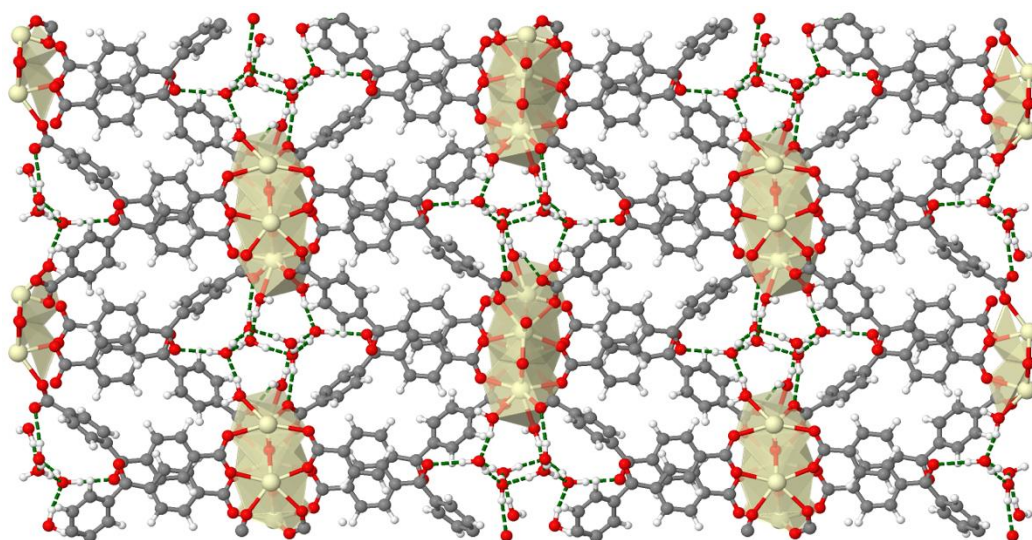
Figure S15. Crystal structure of CAU-58-CDB_wet *pattern-1* obtained at the PBEsol0-3c level of theory. Color scheme: Ce and Ce-O polyhedra = yellow, O = red, C = grey, H = white. The hydrogen-bond network is represented by dashed green lines.
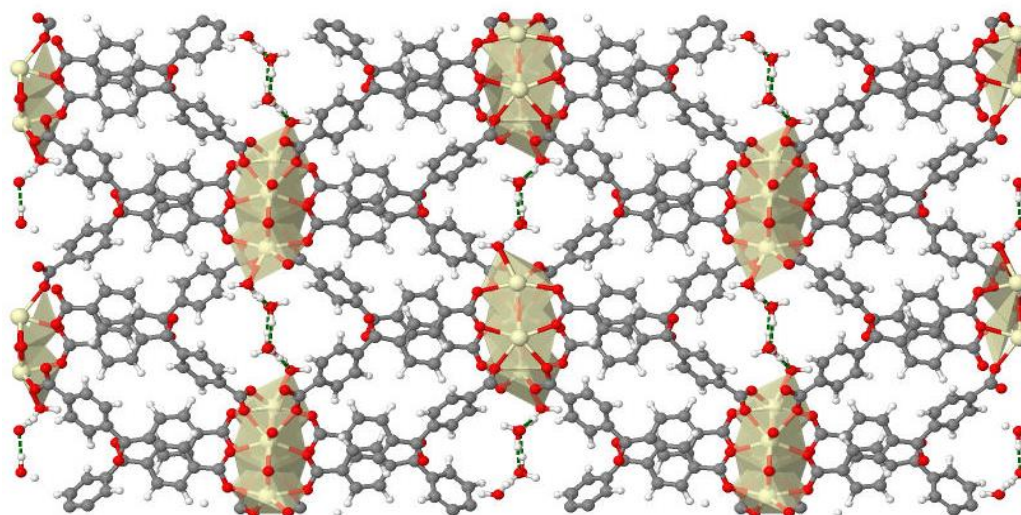

Figure S16. Crystal structure of CAU-58-CDB_wet *pattern-2* obtained at the PBEsol0-3c level of theory. Color scheme: Ce and Ce-O polyhedra = yellow, O = red, C = grey, H = white. The hydrogen-bond network is represented by dashed green lines.

Figure S17. Crystal structure of CAU-58-CDB_dry *pattern-1* obtained at the PBEsol0-3c level of theory. Color scheme: Ce and Ce-O polyhedra = yellow, O = red, C = grey, H = white. The hydrogen-bond network is represented by dashed green lines.

Figure S18. Crystal structure of CAU-58-CDB_dry *pattern-2* obtained at the PBEsol0-3c level of theory. Color scheme: Ce and Ce-O polyhedra = yellow, O = red, C = grey, H = white. The hydrogen-bond network is represented by dashed green lines.
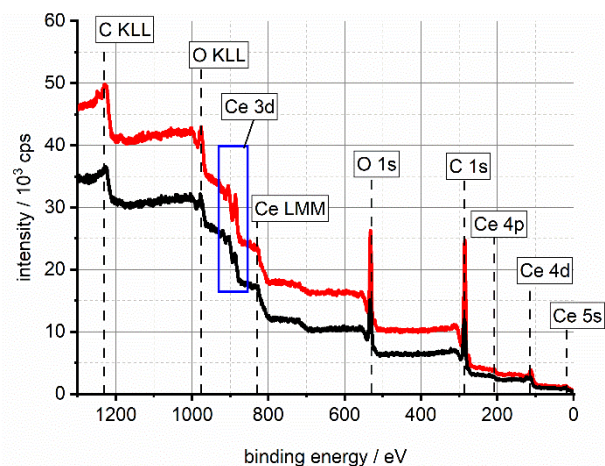
10. X-ray photoelectron spectroscopy

XPS spectra were collected on CAU-58-ODB and CAU-58-CDB. The resulting wide spectra are shown in Figure S19. The respective Ce 3d spectra (blue rectangle) are displayed in Figure 6 of the main manuscript.


Figure S19. XPS wide spectrum of CAU-58-ODB (black) and CAU-58-CDB (red).

11. Thermogravimetric analysis

Thermogravimetric measurements were carried out for CAU-58-ODB and both CAU-58-CDB phases. The results are shown in Figures S20 and S21. The observed and theoretical mass losses are listed in Table S4 and PXRD patterns of the thermal decomposition products after TG analysis are displayed in Figure S22.
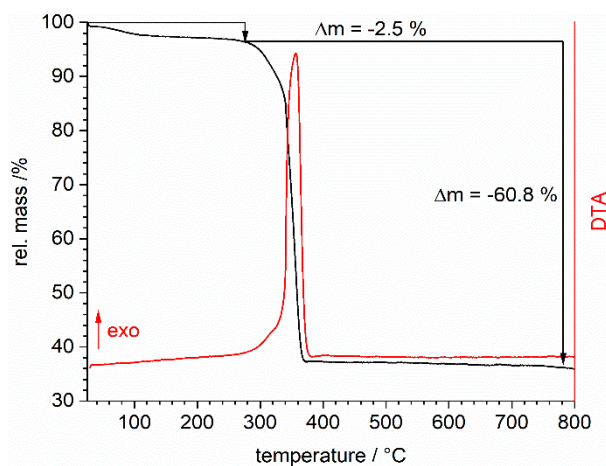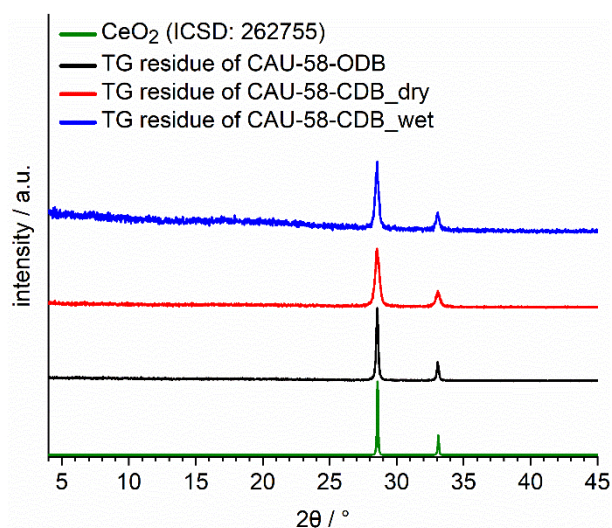

Figure S20. TG- and DTA curve of CAU-58-ODB.
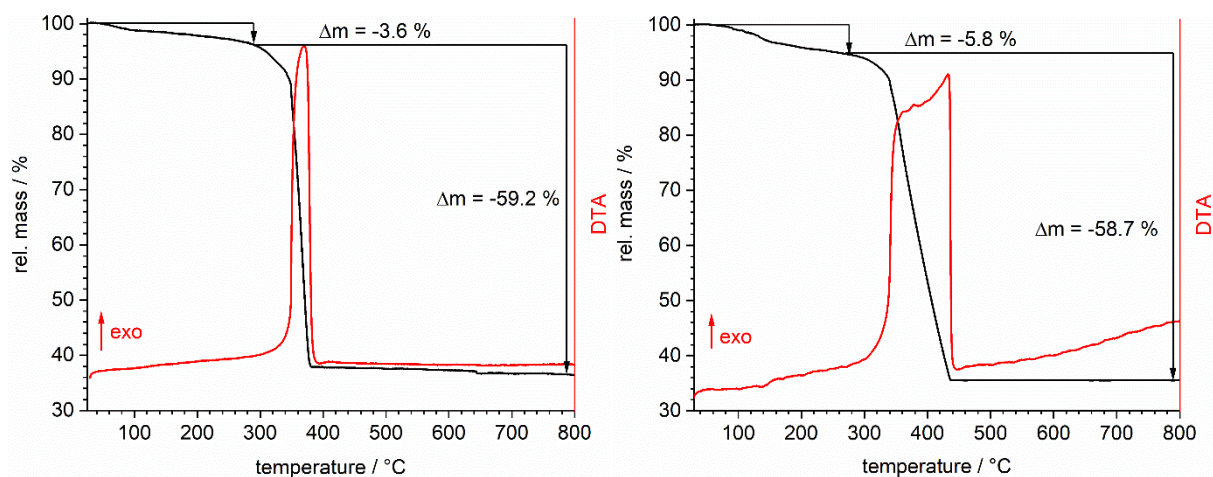
Figure S21. TG- and DTA curves of CAU-58-CDB_dry (left) and CAU-58-CDB_wet (right).

Table S4. Results from the TG analyses for all compounds performed in air.

| Sample	Solvent step		Decomposition step	
	obs. / wt%	H_2O eq. per sum formula	obs. / wt%	calc. / wt%
CAU-58-ODB	2.5	0.7	60.8	55.7
CAU-58-dry	3.6	0.9	59.2	58.4
CAU-58-wet	5.8	1.6	58.7	55.6

Figure S22. PXRD patterns of the thermal decomposition products after TG analysis in comparison to the calculated diffraction pattern of CeO_2.

# 12. Variable temperature powder X-ray diffraction

Variable temperature PXRD data (VT-PXRD) were collected on all MOFs (Fig. S22-S23 and Fig. 7, main manuscript). The temperature range between 30 °C and the decomposition temperatures of the compounds were studied. Samples were heated in steps of 10 or 20 °C (heating rate: 50 °C/min, measurement time: 10 min). Individual patterns from the VT-PXRD measurement of CAU-58-CDB_wet are shown in Figure S25. A transformation to the *as-synthesized* phase CAU-58-CDB_dry is observed.
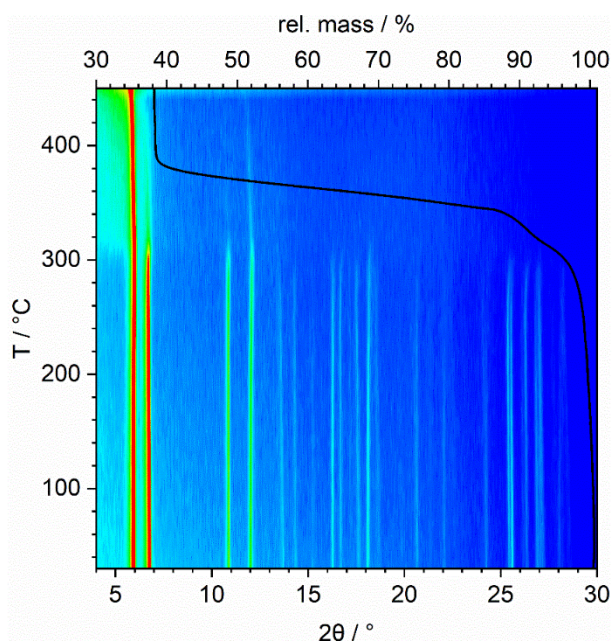
**Figure S23.** Results from the VT-PXRD measurement of CAU-58-ODB with inserted TG data.
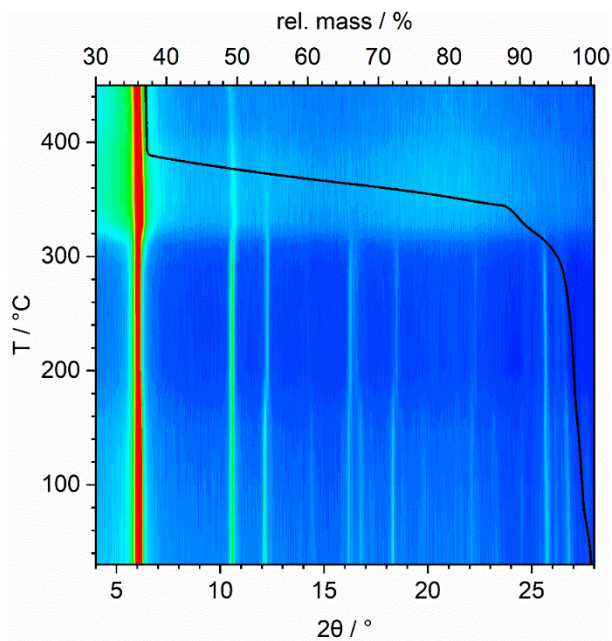
Figure S24. Results from the VT-PXRD measurement of CAU-58-CDB_dry with inserted TG data.
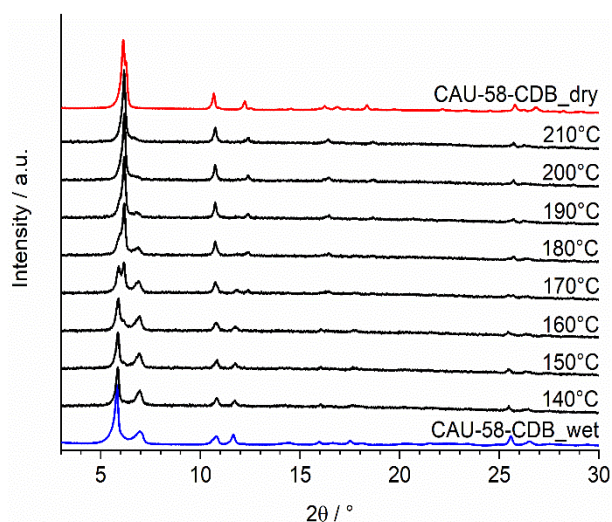
Figure S25. Individual patterns from the VT-PXRD measurement of CAU-58-CDB_wet. Room temperature PXRD patterns of the "wet" and "dry" phases are added for comparison.

13. IR and DRIFT spectroscopy

The IR spectra of both CAU-58 MOFs are shown in Figure S26. IR spectra from the respective bulk linker molecules are added for comparison. In addition, the DRIFTS spectrum of CAU-58-CDB_wet is presented in Figure S27. The sample was heated in air until 460 °C (20 °C steps) and a complete decomposition is observed above 400 °C
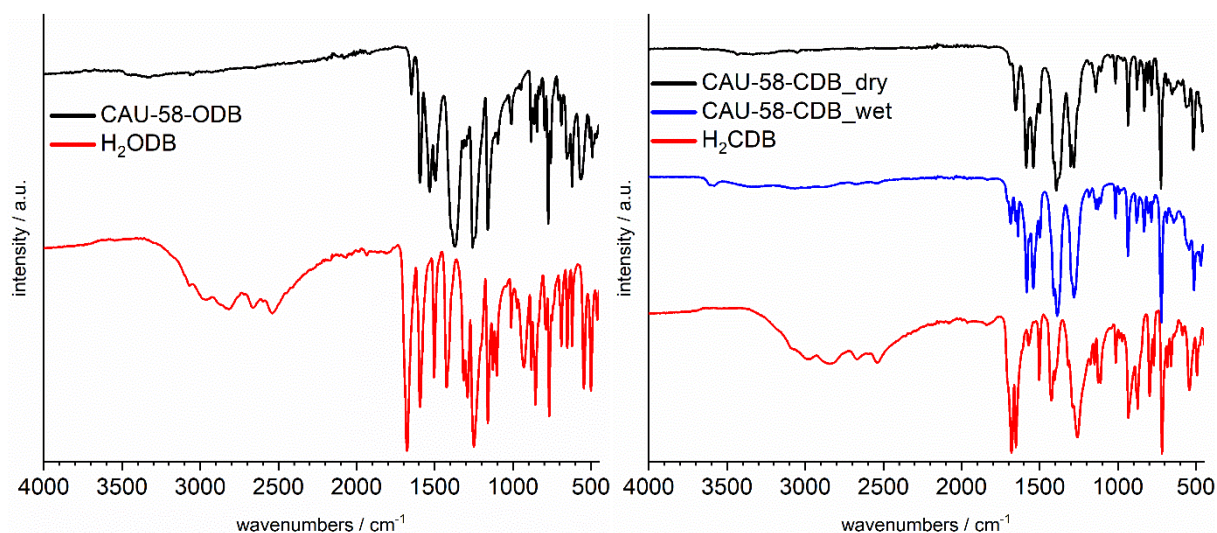
Figure S26. IR spectra of CAU-58-ODB (left) and CAU-58-CDB (right). IR spectra from the bulk linker molecules are added for comparison.
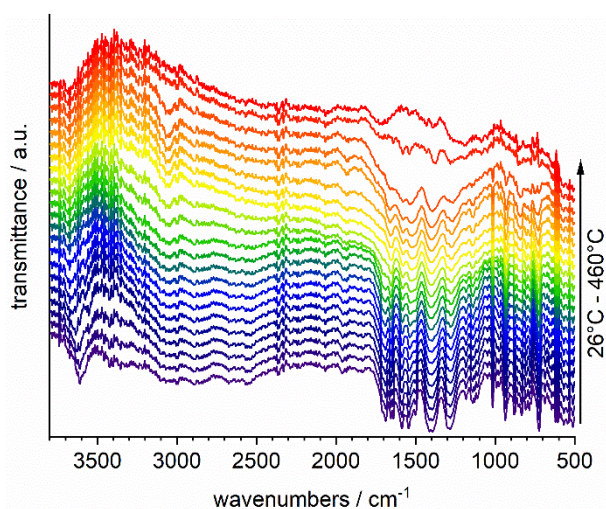
Figure S27. DRIFTS spectrum of CAU-58-CDB_wet. The sample was heated in air until 460 °C (20 °C steps).

14. Sorption measurements

CAU-58-ODB and CAU-58-CDB_dry were characterized by N_2 sorption and H_2O sorption measurements (Fig. S28). All samples were treated for 16 h at a temperature of 210 °C under reduced pressure ($p < 10^{-2}$ mbar) prior to the measurements. The stability of both compounds during activation and sorption measurements was subsequently confirmed by PXRD measurements (Fig. S29)
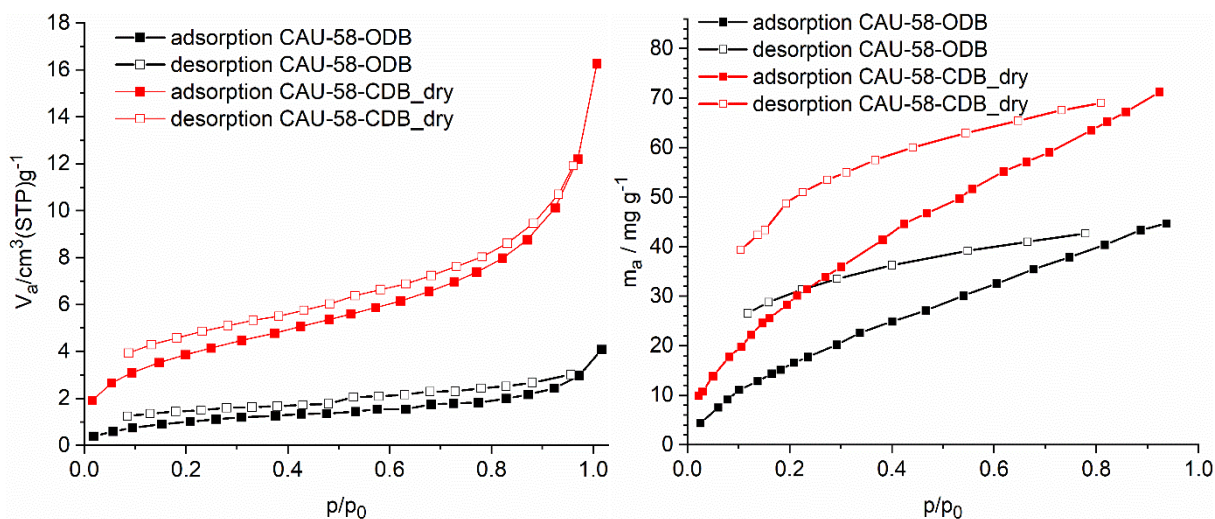
Figure S28. N_2 sorption (left) and H_2O sorption (right) isotherms of CAU-58-ODB (black) and CAU-58-CDB_dry (red).

21
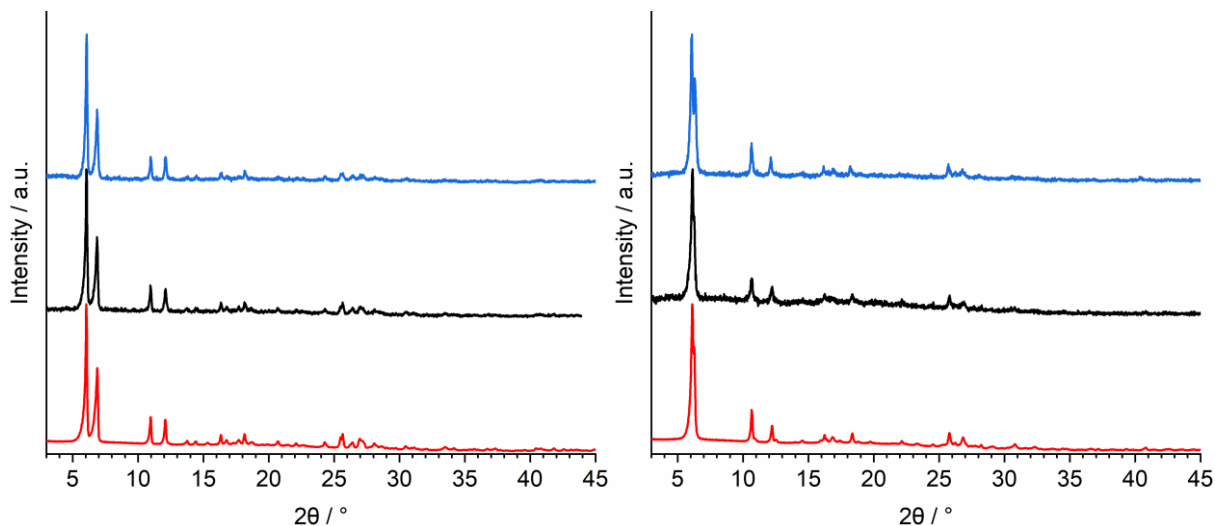
Figure S29. PXRD patterns (λ = 1.5401 Å) of CAU-58-ODB (left) and CAU-58-CDB_dry (right) before (red) and after N_2 sorption (black) or H_2O sorption (blue) measurements.

15. Photocatalytic degradation of methyl orange

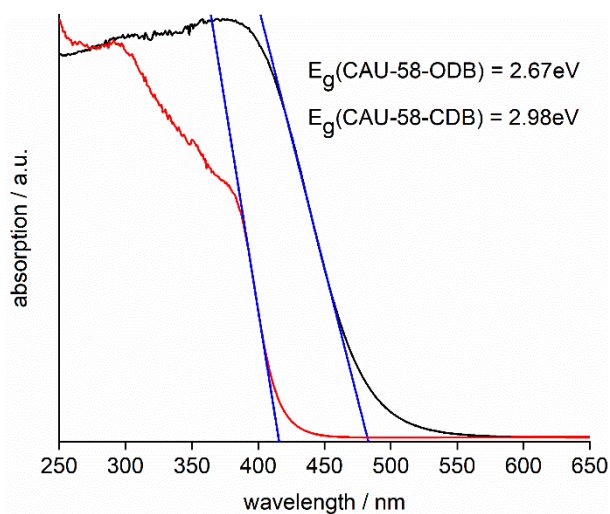UV-Vis spectra of both MOFs are displayed in Figure S30. The spectra were used to calculate the experimental bandgaps (Tauc model).

E_g(CAU-58-ODB) = 2.67eV
E_g(CAU-58-CDB) = 2.98eV

Figure S30. Bandgaps of CAU-58-ODB (black) and CAU-58-CDB (red) were determined from the UV-Vis spectra using the Tauc model.

The MOFs were deployed as catalysts for the photodegradation of methyl orange (MO) under UV light (Fig. S31-S34). Experiments were also performed without irradiation for comparison. The dye content was quantified by UV-Vis spectroscopy at different reaction times and the percentage of degradation was calculated according to equation 3:

$$\%\text{Degradation} = (1 - \frac{\text{Abs}_t}{\text{Abs}_{t_0}}) \cdot 100 \tag{3}$$

22
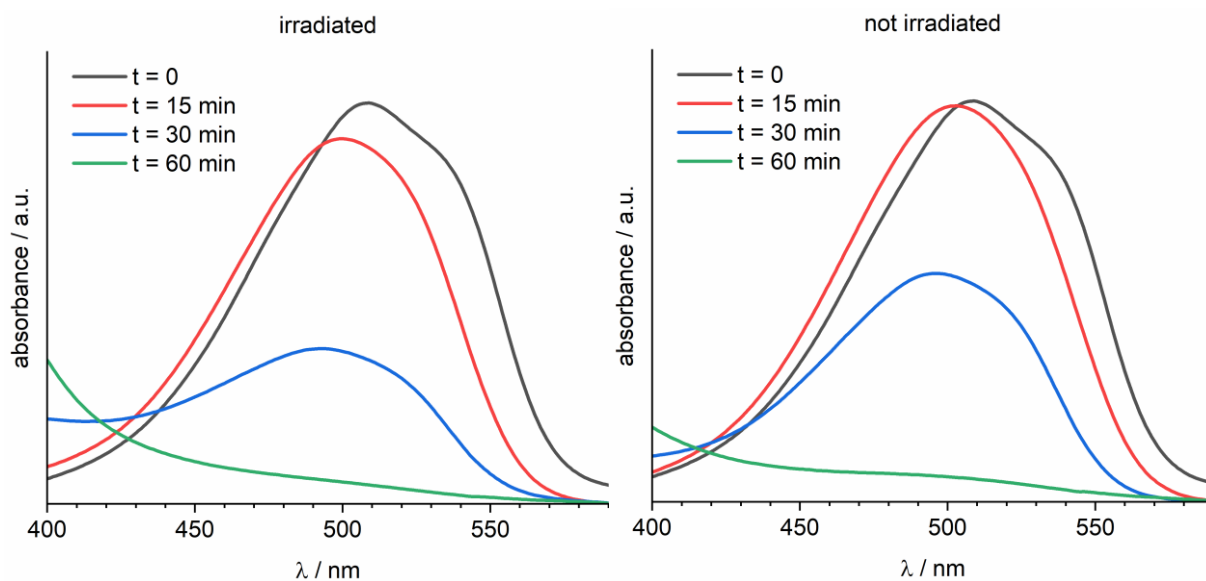
Figure S31. UV-Vis spectra of methyl orange degradation with CAU-58-ODB under irradiated (left) and "dark" conditions (right).
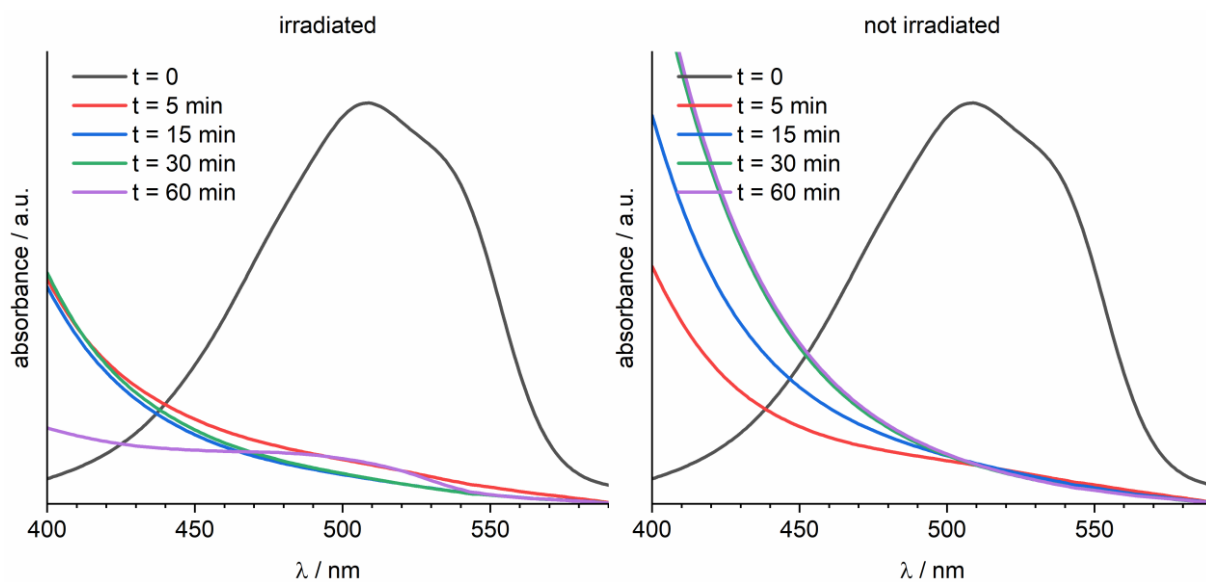
Figure S32. UV-Vis spectra of methyl orange degradation with CAU-58-CDB under irradiated (left) and "dark" conditions (right).
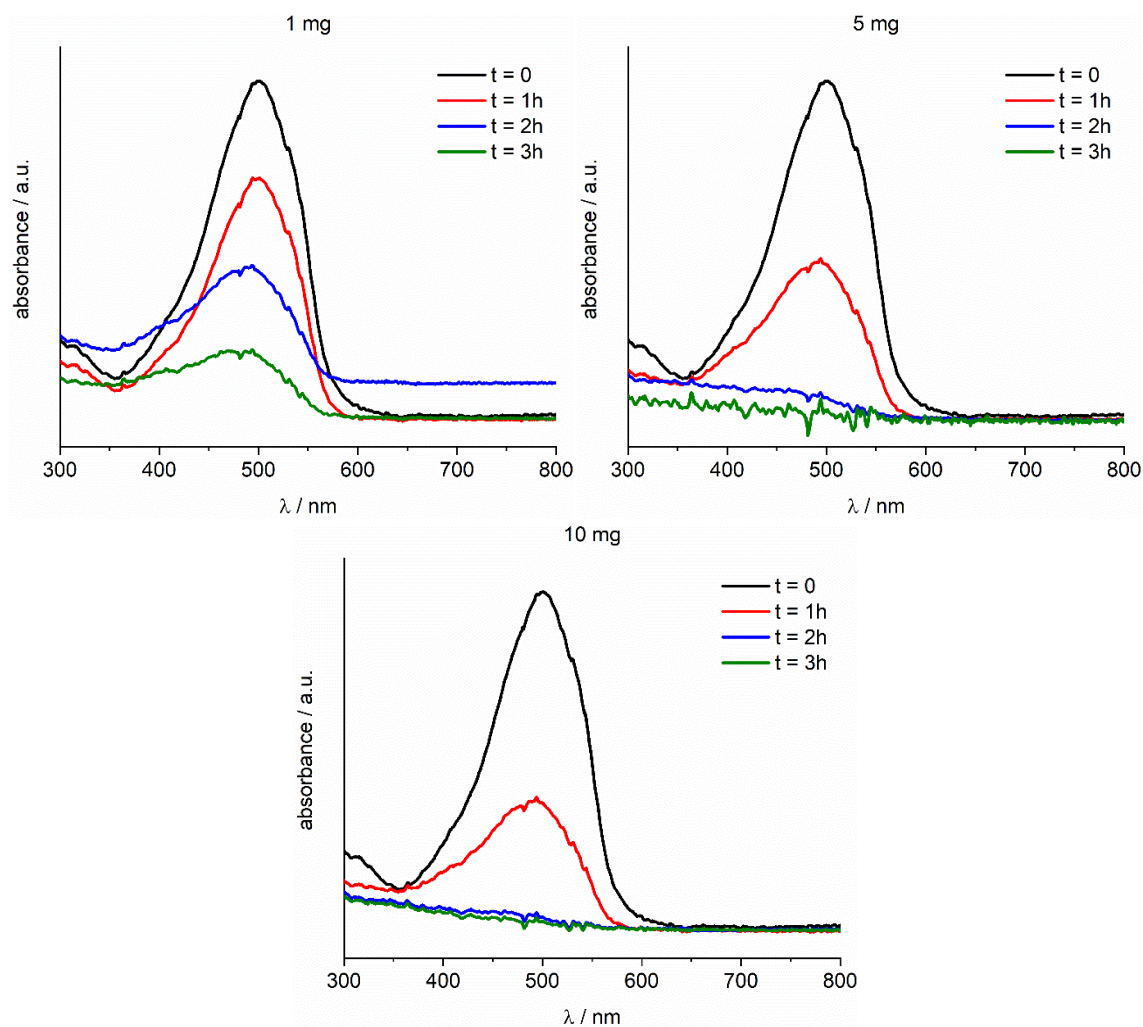
Figure S33. UV-Vis spectra of methyl orange degradation with different amounts of CAU-58-ODB as the catalyst: 1 mg (top left), 5 mg (top right) and 10 mg bottom.
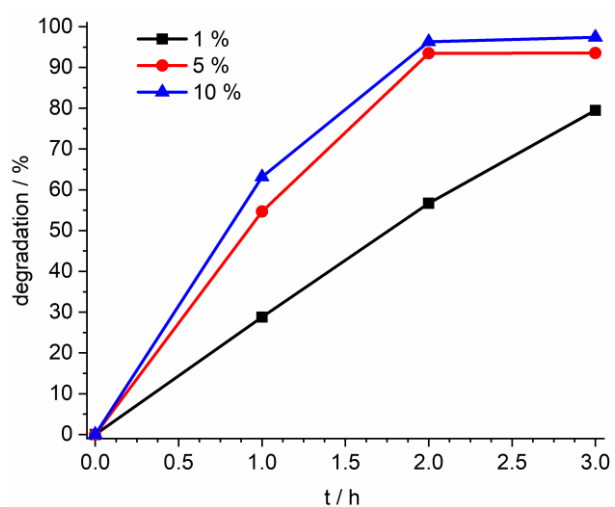
Figure S34. Methyl orange degradation (%) with different amounts of CAU-58-ODB: 1 mg (black), 5 mg (red) and 10 mg (blue).

The probable mechanism for degradation of dyes with Ce(IV) MOFs, was proposed for Ce-UiO-66 by Zhao *et al.*[27] (Fig. S35). The dye molecules are adsorbed on the surface of Ce(IV)-MOF through physisorption (electrostatic/π-π interactions) and/or chemical adsorption (hydrogen/Ce–O bonding). Under irradiation with UV-light the photoinduced electron-hole couple is generated due to the LMCT mechanism. An electron is transferred from the Ce(IV) valence band (VB) to the linker conduction band (CB). Photo-induced electrons from the CB on the MOF surface react with absorbed O_2 molecules to form superoxide anion radicals O_2^-. In addition, holes generated from the VB of the Ce(IV) ions can react with H_2O to form reactive $^{\cdot}OH$ molecules. These two reactive species could then effectively decompose adsorbed methyl orange into smaller molecules.
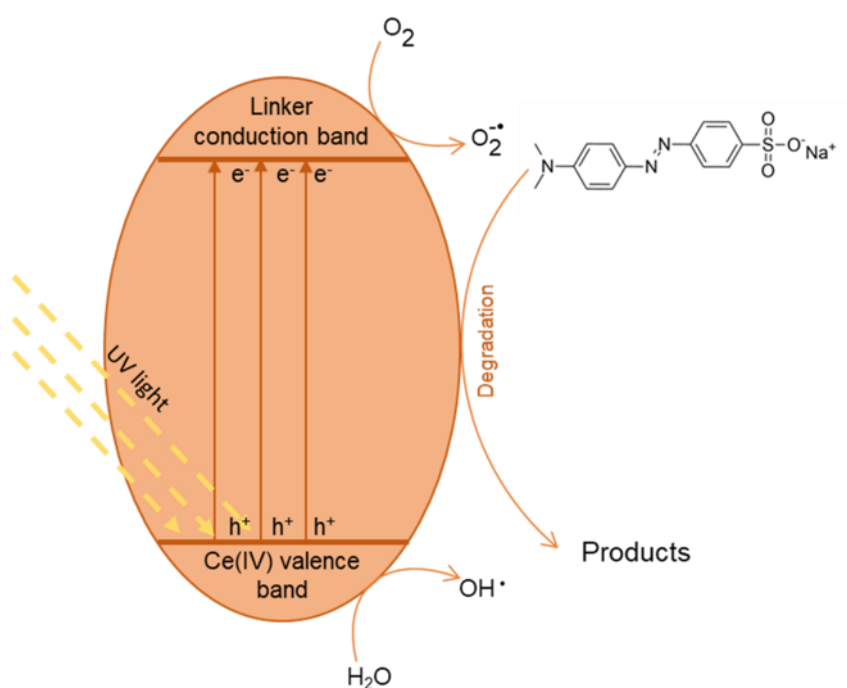
Figure S35. Proposed mechanism for degradation of MO with Ce(IV) MOFs.

16. Scanning electron microscopy

Both CAU-58 MOFs were further studied by scanning electron microscopy (Fig. S36). Samples were sputtered with gold prior to the measurement to enhance conductivity and resolution.
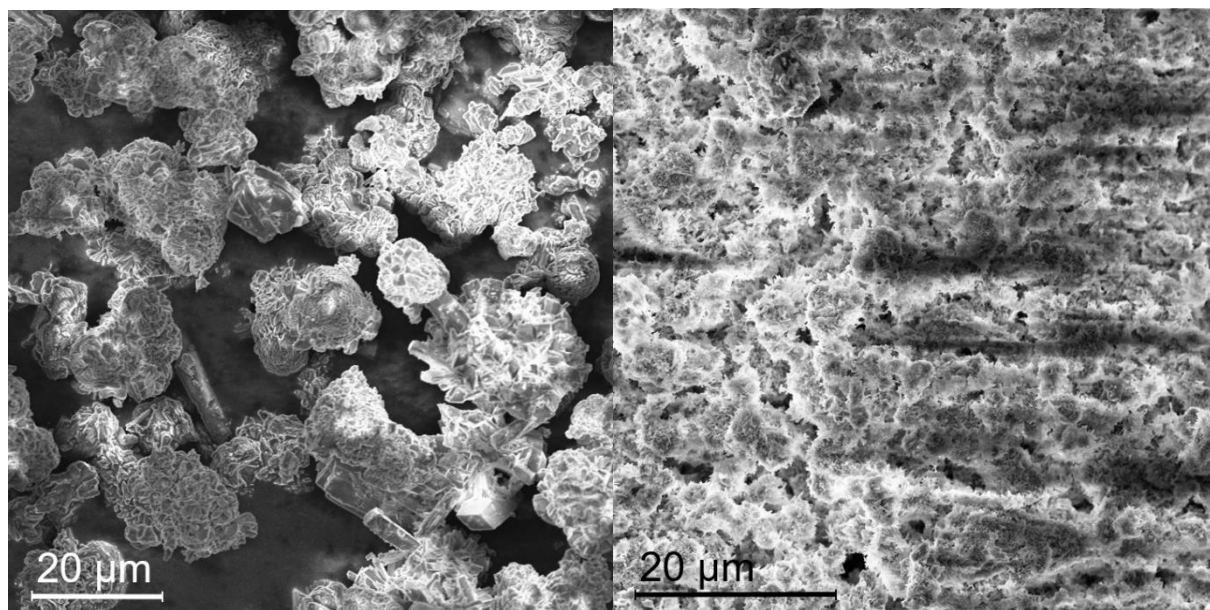
Fig. S36. Scanning electron micrographs of CAU-58-ODB (left) and CAU-58-CDB (right). Samples were previously sputtered with gold to enhance conductivity and resolution.

17. XANES measurements
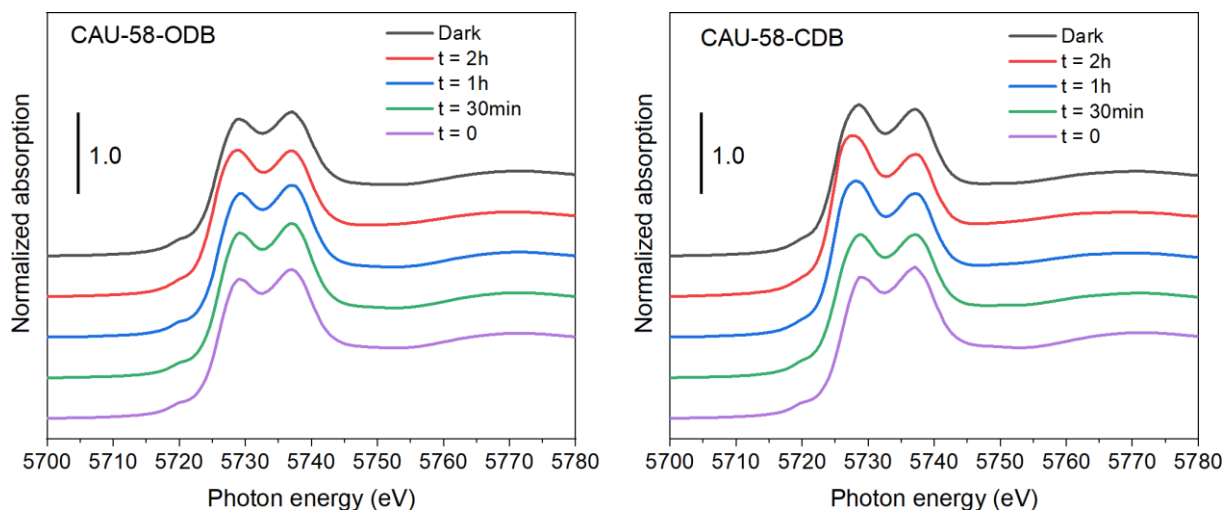
Figure S37. *Ex situ* Ce L_3-edge XANES spectra of solid CAU-58-ODB (left) and CAU-58-CDB (right) that catalyzed the reaction of MO photodegradation for different reaction times. "Dark" spectra correspond to the materials that underwent the 2-hour reaction without irradiation.

Table S5. Results of the linear combination analysis of Ce L$_3$-edge XANES spectra of the solid CAU-58-ODB and CAU-58-CDB MOFs after the photodegradation reaction of MO. The spectrum of Ce(NO$_3$)$_3$ was used as Ce(III) reference, whereas the spectra of each MOF at t = 0 was employed as Ce(IV) references. Reported errors are purely statistical, the real error is estimated to be around 3 %.

Stage	CAU-58-ODB		CAU-58-CDB	
	Ce(III) fraction/ %	R-factor	Ce(III) fraction/ %	R-factor
t = 30 min	0 ± 1	0.0021	11 ± 1	0.0005
t = 1 h	0 ± 2	0.0013	21 ± 1	0.0105
t = 2 h	12 ± 1	0.0040	27 ± 1	0.0155
Dark	4 ± 1	0.0002	15 ± 2	0.0059

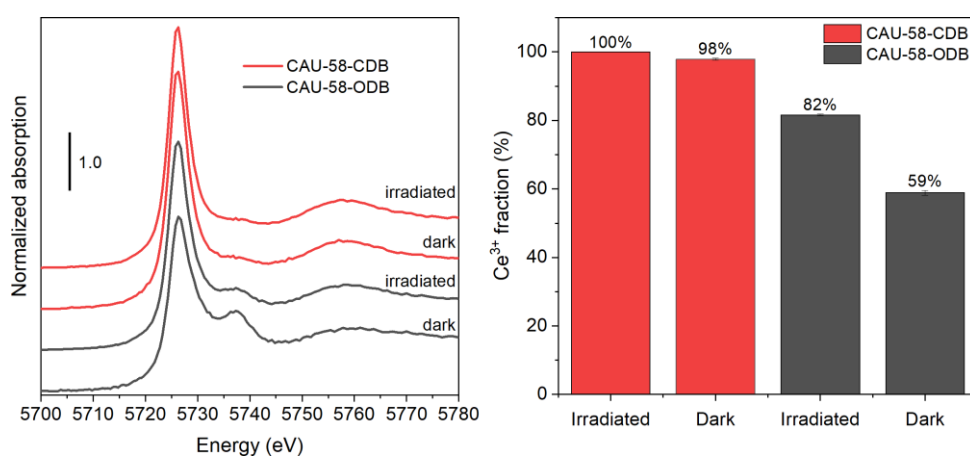**Figure S38.** Ce L$_3$-edge XANES spectra of the reaction solutions after the MO degradation catalyzed by CAU-58-ODB and CAU-58-CDB for 2 h with and without irradiation (left) and the corresponding quantification of the Ce(III) fraction (right).

Table S6. Results of the linear combination analysis of Ce L$_3$-edge XANES spectra of the reaction solutions after the MO degradation catalyzed by CAU-58-ODB and CAU-58-CDB for 2 h with and without UV irradiation. The spectrum of the solution after the reaction of CAU-58-CDB upon irradiation was used as Ce(III) reference, whereas the spectra of solid MOFs at t = 0 (before reaction) were employed as Ce(IV) references. Reported errors are purely statistical, the real error is estimated to be around 5 %.

Spectrum	CAU-58-ODB		CAU-58-CDB	
	Ce(III) fraction / %	R-factor	Ce(III) fraction / %	R-factor
Irradiated	82 ± 1	0.0005	100*	n/a*
Dark	59 ± 1	0.0059	98 ± 1	0.0007

*The spectrum was used as the Ce(III) reference.

18. References

(1) Damm, M.; Kappe, C. O. Parallel Microwave Chemistry in Silicon Carbide Reactor Platforms: An in-Depth Investigation into Heating Characteristics. *Mol Divers* **2009**, *13* (4), 529–543. https://doi.org/10.1007/s11030-009-9167-3.

(2) Mathon, O.; Beteva, A.; Borrel, J.; Bugnazet, D.; Gatla, S.; Hino, R.; Kantor, I.; Mairs, T.; Munoz, M.; Pasternak, S.; Perrin, F.; Pascarelli, S. The Time-Resolved and Extreme Conditions XAS (TEXAS) Facility at the European Synchrotron Radiation Facility: The General-Purpose EXAFS Bending-Magnet Beamline BM23. *J Synchrotron Rad* **2015**, *22* (6), 1548–1554. https://doi.org/10.1107/S1600577515017786.

(3) Klementiev, K.; Chernikov, R. XAFSmass: A Program for Calculating the Optimal Mass of XAFS Samples. *J. Phys.: Conf. Ser.* **2016**, *712*, 012008. https://doi.org/10.1088/1742-6596/712/1/012008.

(4) Ravel, B.; Newville, M. *ATHENA* , *ARTEMIS* , *HEPHAESTUS* : Data Analysis for X-Ray Absorption Spectroscopy Using *IFEFFIT*. *J Synchrotron Rad* **2005**, *12* (4), 537–541. https://doi.org/10.1107/S0909049505012719.

(5) Fairley, N.; Fernandez, V.; Richard-Plouet, M.; Guillot-Deudon, C.; Walton, J.; Smith, E.; Flahaut, D.; Greiner, M.; Biesinger, M.; Tougaard, S.; Morgan, D.; Baltrusaitis, J. Systematic and Collaborative Approach to Problem Solving Using X-Ray Photoelectron Spectroscopy. *Applied Surface Science Advances* **2021**, *5*, 100112. https://doi.org/10.1016/j.apsadv.2021.100112.

(6) Cichocka, M. O.; Ångström, J.; Wang, B.; Zou, X.; Smeets, S. High-Throughput Continuous Rotation Electron Diffraction Data Acquisition via Software Automation. *Journal of Applied Crystallography* **2018**, *51* (6), 1652–1661. https://doi.org/10.1107/s1600576718015145.

(7) Kabsch, W. *XDS. Acta Crystallographica Section D Biological Crystallography* **2010**, *66* (2), 125–132. https://doi.org/10.1107/S0907444909047337.

(8) Sheldrick, G. M. SHELXT - Integrated Space-Group and Crystal-Structure Determination. *Acta Crystallographica Section A: Foundations of Crystallography* **2015**, *71* (1), 3–8. https://doi.org/10.1107/S2053273314026370.

(9) Sheldrick, G. M. A Short History of SHELX. *Acta Crystallographica Section A: Foundations of Crystallography* **2008**, *64* (1), 112–122. https://doi.org/10.1107/S0108767307043930.

(10) Burla, M. C.; Caliandro, R.; Carrozzini, B.; Cascarano, G. L.; Cuocci, C.; Giacovazzo, C.; Mallamo, M.; Mazzone, A.; Polidori, G. Crystal Structure Determination and Refinement via SIR2014. *Journal of Applied Crystallography* **2015**, *48* (1), 306–309. https://doi.org/10.1107/S1600576715001132.

(11) Coelho, A. A. TOPAS and TOPAS-Academic: An Optimization Program Integrating Computer Algebra and Crystallographic Objects Written in C++. *J Appl Cryst* **2018**, *51* (1), 210–218. https://doi.org/10.1107/S1600576718000183.

(12) Lammert, M.; Wharmby, M. T.; Smolders, S.; Bueken, B.; Lieb, A.; Lomachenko, K. A.; Vos, D. D.; Stock, N. Cerium-Based Metal Organic Frameworks with UiO-66 Architecture: Synthesis, Properties and Redox Catalytic Activity. *Chem. Commun.* **2015**, *51* (63), 12578–12581. https://doi.org/10.1039/C5CC02606G.

(13) D'Amato, R.; Donnadio, A.; Carta, M.; Sangregorio, C.; Tiana, D.; Vivani, R.; Taddei, M.; Costantino, F. Water-Based Synthesis and Enhanced CO_2 Capture Performance of Perfluorinated Cerium-Based Metal–Organic Frameworks with UiO-66 and MIL-140 Topology. *ACS Sustainable Chem. Eng.* **2019**, *7* (1), 394–402. https://doi.org/10.1021/acssuschemeng.8b03765.

(14) Gu, J.; Chen, H.; Ren, Y.; Gu, Z.; Li, G.; Xu, W.; Yang, X.; Wen, J.; Wu, J.; Jin, H. A Novel Cerium(IV)-Based Metal-Organic Framework for CO_2 Chemical Fixation and Photocatalytic Overall Water Splitting. *ChemSusChem* **2022**, *15* (1). https://doi.org/10.1002/cssc.202102368.

(15) Schoedel, A.; Li, M.; Li, D.; O'Keeffe, M.; Yaghi, O. M. Structures of Metal–Organic Frameworks with Rod Secondary Building Units. *Chem. Rev.* **2016**, *116* (19), 12466–12535. https://doi.org/10.1021/acs.chemrev.6b00346.

(16) Blatov, V. A.; Shevchenko, A. P.; Proserpio, D. M. Applied Topological Analysis of Crystal Structures with the Program Package ToposPro. *Crystal Growth & Design* **2014**, *14* (7), 3576–3586. https://doi.org/10.1021/cg500498k.

(17) Delgado-Friedrichs, O.; O'Keeffe, M. Identification of and Symmetry Computation for Crystal Nets. *Acta Cryst A* **2003**, *59* (4), 351–360. https://doi.org/10.1107/S0108767303012017.

(18) Doná, L.; Brandenburg, J. G.; Civalleri, B. Extending and Assessing Composite Electronic Structure Methods to the Solid State. *J. Chem. Phys.* **2019**, *151* (12), 121101. https://doi.org/10.1063/1.5123627.

(19) Kruse, H.; Grimme, S. A Geometrical Correction for the Inter- and Intra-Molecular Basis Set Superposition Error in Hartree-Fock and Density Functional Theory Calculations for Large Systems. *J. Chem. Phys.* **2012**, *136* (15), 154101. https://doi.org/10.1063/1.3700154.

(20) Brandenburg, J. G.; Alessio, M.; Civalleri, B.; Peintinger, M. F.; Bredow, T.; Grimme, S. Geometrical Correction for the Inter- and Intramolecular Basis Set Superposition Error in Periodic Density Functional Theory Calculations. *J. Phys. Chem. A* **2013**, *117* (38), 9282–9292. https://doi.org/10.1021/jp406658y.

(21) Grimme, S.; Antony, J.; Ehrlich, S.; Krieg, H. A Consistent and Accurate Ab Initio Parametrization of Density Functional Dispersion Correction (DFT-D) for the 94 Elements H-Pu. *J. Chem. Phys.* **2010**, *132* (15), 154104. https://doi.org/10.1063/1.3382344.

(22) Grimme, S.; Ehrlich, S.; Goerigk, L. Effect of the Damping Function in Dispersion Corrected Density Functional Theory. *Journal of Computational Chemistry* **2011**, *32* (7), 1456–1465. https://doi.org/10.1002/jcc.21759.

(23) Donà, L.; Brandenburg, J. G.; Bush, I. J.; Civalleri, B. Cost-Effective Composite Methods for Large-Scale Solid-State Calculations. *Faraday Discuss.* **2020**, *224* (0), 292–308. https://doi.org/10.1039/D0FD00066C.

(24) Möslein, A. F.; Donà, L.; Civalleri, B.; Tan, J.-C. Defect Engineering in Metal–Organic Framework Nanocrystals: Implications for Mechanical Properties and Performance. *ACS Appl. Nano Mater.* **2022**, *5* (5), 6398–6409. https://doi.org/10.1021/acsanm.2c00493.

(25) Souza, B. E.; Donà, L.; Titov, K.; Bruzzese, P.; Zeng, Z.; Zhang, Y.; Babal, A. S.; Möslein, A. F.; Frogley, M. D.; Wolna, M.; Cinque, G.; Civalleri, B.; Tan, J.-C. Elucidating the Drug Release from Metal–Organic Framework Nanocomposites via In Situ Synchrotron Microspectroscopy and Theoretical Modeling. *ACS Appl. Mater. Interfaces* **2020**, *12* (4), 5147–5156. https://doi.org/10.1021/acsami.9b21321.

(26) Xiong, T.; Zhang, Y.; Donà, L.; Gutiérrez, M.; Möslein, A. F.; Babal, A. S.; Amin, N.; Civalleri, B.; Tan, J.-C. Tunable Fluorescein-Encapsulated Zeolitic Imidazolate Framework-8 Nanoparticles for Solid-State Lighting. *ACS Appl. Nano Mater.* **2021**, *4* (10), 10321–10333. https://doi.org/10.1021/acsanm.1c01829.

(27) Zhao, D.; Cai, C. Cerium-Based UiO-66 Metal-Organic Framework for Synergistic Dye Adsorption and Photodegradation: A Discussion of the Mechanism. *Dyes and Pigments* **2021**, *185*, 108957. https://doi.org/10.1016/j.dyepig.2020.108957.